ANDICAM I and J-band monitoring of bright inner Galactic late-type stars.

Maria Messineo[1,2]

[1]Key Laboratory for Researches in Galaxies and Cosmology, University of Science and Technology of China, Chinese Academy of Sciences, Hefei, Anhui, 230026, China

[2] ASTROMAGIC freelancer, Potsdam 14482, Germany

Received ⟨reception date⟩; Accepted ⟨acception date⟩

Abstract

Time-series photometry in I- and J-band of 57 inner Galactic late-type stars, highly-probable red supergiant (RSG) stars, is here presented. 38% of the sample presents significant photometric variations. The variations in I- and J-band appear to be correlated, with $\Delta I \propto \Delta J \times 2.2$, ΔI variations ranging from 0.04 to 1.08 mag, ΔJ variations from 0.03 mag 0.52 mag. New short periods (< 1000 d) could be estimated for 8 stars and range from 167 to 433 d. This work confirms that the sample is not contaminated by large amplitude Asymptotic Giant Branch (AGB) stars. Furthermore, despite the large errors in distance, the period-luminosity diagram suggests that the sample is populating the same sequence as the known Galactic RSGs.

Key words: stars: evolution — stars: supergiants — stars: massive

1 Introduction

Red supergiant (RSG) stars are late-type stars burning helium in the central core and with initial masses larger than 8-9 $M_{\odot}$. They are intrinsically bright at infrared wavelengths and, in principle, they can be detected at great distances even in the most obscured regions of the Galaxy. Unfortunately, the resemblance between RSGs and Asymptotic Giant Branch (AGB) stars and the lack of precise distances complicate their detection.

In the last decade, the astronomical community has made a great effort to conduct medium and high-resolution spectroscopic studies of RSGs. Nowadays, metallicity and temperatures can be directly inferred from iron lines (e.g., Taniguchi et al. 2021), and some infrared lines have been found with strengths that correlate with the stellar luminosity (e.g., Messineo et al. 2021). The spectroscopic future looks promising with millions of spectra to be released by the Gaia, LAMOST, GALAH, and 4MOST, surveys (e.g., de Jong et al. 2012; Gaia Collaboration et al. 2021; Sharma et al. 2022; Wu et al. 2021). This will allow us to greatly improve the census of Galactic RSGs and to better learn how to classify them well and at minimum cost.

For improved Galactic distances, one must wait for the new releases of Gaia parallaxes and the pulsational periods of long-period variable stars. Periods for millions of stars will soon be available from the Gaia survey and the forthcoming LSST survey (Ivezić et al. 2019). Periods may yield distance estimates via a period-luminosity relation.

It has long been established that there is a correlation between the length of the period and the stellar luminosity of variable late-type stars. That such a relation also exists for variable RSG stars was noticed by Glass (1979) by analyzing seven RSGs in the LMC. The work in the LMC by Feast et al. (1980) confirmed it with the analysis of 24 RSGs analyzed. The RSG absolute K magnitudes ($M_{\rm K}$) versus Periods (Per) relation falls above that of AGB stars, and their K-band amplitudes are typically smaller than 0.25 mag, while in AGB stars amplitudes range from 0.5 to 1.0 mag (Wood et al. 1983). Starting around the end of the 90s, the description of the long-period variables became more complicated with the discovery of several parallel sequences of pulsators in the LMC (Ita et al. 2004) and multi frequencies detected in their light-curves (e.g., Soszyński & Wood 2013). In the M33 galaxy, Soraisam et al. (2018) detected a well-defined period-luminosity relation for RSGs pulsating in the fundamental mode, and a parallel sequence, likely, of first-overtone pulsators 0.3 mag brighter.

In the Milky Way, Pierce et al. (2000) report that 12 RSGs in the Perseus OB1 association follow the same period-luminosity relations determined for RSGs in the LMC and M33 in R, I, K-bands. Kiss et al. (2006) analyze the light-curves of about 40 Galactic M-type RSGs covering 61 years and found that about 40% of them have two periods, a short period (< 1000 d) and a long secondary period (LSP) greater than 1000 d. The same sample of Galactic stars and others from the LMC and M33 (220 stars) were analyzed by Chatys et al. (2019), to find that, for variable RSGs, a period-luminosity exists for the short periods and it appears to be universal and independent of metallicity. About 52% of the Galactic RSG sample has short periods and 47% long periods.

In the last decade, a large number of new Galactic RSGs have been reported in the literature (e.g., Dorda et al. 2018; Messineo et al. 2017). At the current time, in view of the forthcoming surveys, it is advisable to aim for a more precise and well-established characterization of already detected objects, as those will constitute the reference frames for the new stars to be classified. Especially for those located towards the densest and obscured regions of the Milky Way, variability studies are of primary importance to confirm their nature, estimate their distance, and, therefore, their luminosity class.

2 The sample

The 57 late-type stars observed with ANDICAM are taken from the sample of 94 stars analyzed by Messineo et al. (2016) and Messineo et al. (2017).

The sample of Messineo et al. (2016) comprises stars from the GLIMPSE I North survey brighter than K_s= 7 mag and with A_{K_s}> 0.4 mag, which satisfies the infrared color criteria advised by Messineo et al. (2012). Messineo et al. (2017) show that large equivalent widths of the CO at 2.29 μm (EW(CO) > 45 Å) and lack of water vapour absorption featured 62% of that sample. The sample is, therefore, mostly made up of red supergiants (RSGs) (see discussion in Messineo et al. 2017).

The subsample observed with ANDICAM is listed in Table 1, and comprises 55 stars with broad EW(CO) (> 45 Å) and little water, which Messineo et al. (2017) label as "EW>", plus two other stars (MZM7 and MZM21), which are labeled as "CO" by having EW(CO) larger than 37 Å.

Unfortunately, as described in the recent work of Messineo et al. (2021)[1], the EW(CO) alone is not a good luminosity indicator and distance estimates and variability information remain essential to determine the luminosity class.

In the following, the stars are called late-type stars, as their classification is based on the EW of the CO band-heads at 2.29 μm from low-resolution spectra. A more solid classification can be foreseen with high-resolution spectra. However, the broadness of the EW(CO), together with the lack of water absorption, current distance uncertainty, and the small amplitudes here presented, suggest that they are all consistent with being RSGs.

2.1 Infrared photometry and distances

The collection of infrared photometric measurements and bolometric magnitudes are presented in the works of Messineo et al. (2017) and Messineo & Brown (2019) and listed in Table 1.

In Messineo et al. (2016), distances are determined by comparing the target extinction with the extinction curves of nearby clump stars, which are primary indicators of distance. In Messineo & Brown (2019), Gaia DR2 parallaxes are matched to the infrared sources and used to infer their distances. A revised version of this Gaia catalog with EDR3 parallaxes was made available by Messineo

[1] There is no overlap between the ANDICAM sources and the sources in Messineo et al. (2021)

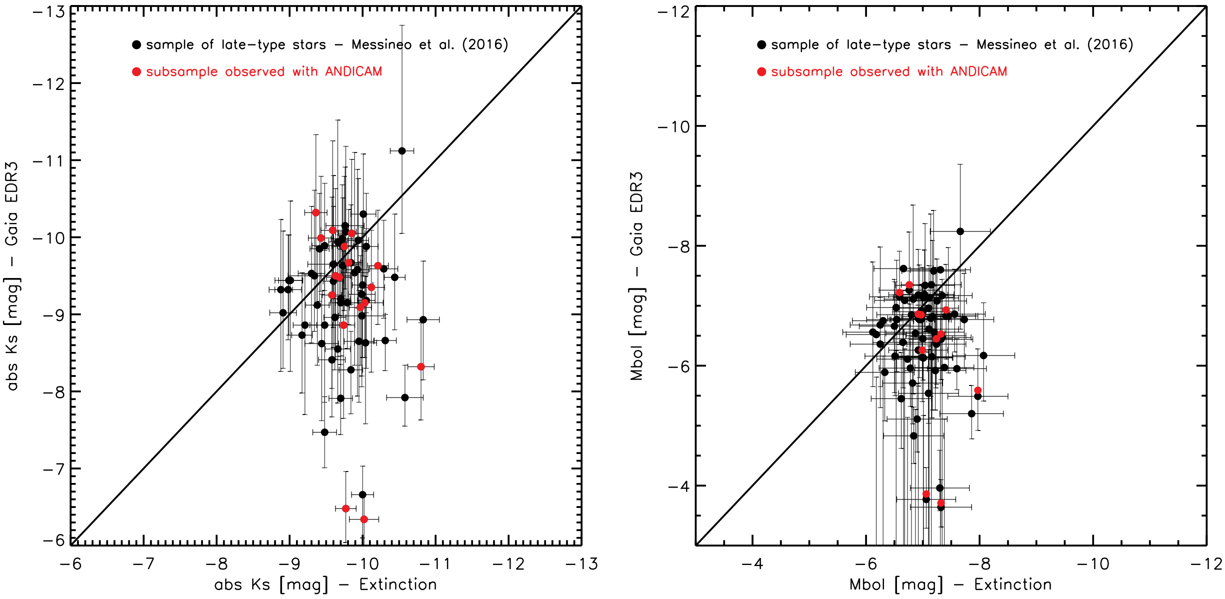

Fig. 1. *Right panel:* Sample of highly-likely M-type RSGs reported by Messineo et al. (2016) and Messineo et al. (2017). The subsample observed with ANDICAM is marked in red. The absolute K_s magnitudes, M_K, calculated with Gaia EDR3 parallaxes (Messineo & Brown 2021) are plotted vs. those based on extinction calculations (Messineo et al. 2016, 2017). *Left panel:* The M_{bol} values calculated with Gaia EDR3 parallaxes (Messineo & Brown 2021) are plotted vs. those based on extinction calculations (Messineo et al. 2016, 2017).

& Brown (2021). Kinematic distances using the Gaia DR2 velocities are only possible for seven sources. The absolute magnitudes in K_s, M_K, are calculated as K_s-A_{K_s}-DM, where Ks are the 2MASS Ks magnitudes A_{K_s} is the interstellar extinction, which is derived from the observed $H-Ks$ and $J-Ks$, by assuming the intrinsic colors of Koornneef (1983) and the extinction coefficients by Messineo et al. (2005), which assumes an infrared power law with an index of -1.9. DM is the distance moduli from the Gaia EDR3 parallaxes.

Unfortunately, fractional parallactic errors are large for this type of cool sources and distances, with resulting errors in the distance moduli mostly between 0.8 and 1.0 mag. However, a comparison with the values inferred using the extinction is interesting because it further confirms the source location in the inner Galaxy, as shown in Fig. 1. The final Gaia release will narrow down these errors.

3 Observations

To monitor the fluxes of the 57 late-type stars, the infrared ANDICAM camera mounted on the 1.3m telescope of Cerro Tololo in Chile was used. The telescope is operated by the SMARTS consortium, and a total of 28.7 nights were allocated to this program (2016B-0106) by the Telescope Allocation Committees (TAC) for the National Optical Astronomy Observatory. A CCD camera was attached for simultaneous optical observations.

Table 1. List of observed late-type stars and parameters from literature.

2MASS-ID	MZM-ID	RSG-Sp	A_{K_s} [mag]	DM [mag]	RUWE	frac [%]	DM2 [mag]	DM3 [mag]	K_{so} [mag]	Ampl(1) [mag]	Ampl(2) [mag]	Per(2) [d]
18112728-175014	MZM4	M0.5	1.38	$12.71^{0.88}_{-0.93}$	2.1	0.4	..	$13.58^{0.12}_{0.12}$	3.53 ± 0.02	0.08	..	..
18114736-192915	MZM5	M2	1.66	$13.22^{1.64}_{-1.30}$	1.3	0.2	..	$13.57^{0.15}_{0.15}$	3.64 ± 0.03	..	..	..
18131562-180122	MZM6	M1	1.13	$13.81^{0.83}_{-0.91}$	..	-0.9	..	$13.68^{0.17}_{0.17}$	3.93 ± 0.03	..	..	..
18132341-185818	MZM7	K4	1.54	$13.07^{0.92}_{-0.65}$	1.1	1.2	..	$13.57^{0.13}_{0.13}$	3.87 ± 0.03	..	..	..
18134914-184633	MZM9	M0	1.27	$12.90^{0.80}_{-0.69}$	1.2	1.0	..	$13.45^{0.14}_{0.14}$	3.75 ± 0.02	..	..	..
18140682-190620	MZM10	M0.5	1.10	$13.51^{0.80}_{-0.69}$	..	0.8	..	$13.65^{0.18}_{0.18}$	3.84 ± 0.03	0.09	..	..
18144593-173754	MZM11	M1	1.88	$8.68^{0.95}_{-0.64}$	2.8	2.7	..	..	3.43 ± 0.03	..	..	..
18154112-164645	MZM16	M1.5	1.05	$12.06^{0.73}_{-0.62}$	1.1	2.2	..	..	4.00 ± 0.02	..	..	..
18155832-165827	MZM17	M0.5	1.54	$13.30^{1.08}_{-1.13}$	1.3	0.7	..	$13.43^{0.20}_{0.20}$	3.80 ± 0.03	..	..	..
18171598-140554	MZM20	M0.5	0.91	$13.34^{1.20}_{-1.56}$	1.2	2.1	..	$13.69^{0.18}_{0.18}$	3.80 ± 0.02	..	..	..
18172865-163739	MZM21	K5.5	1.29	$12.92^{0.72}_{-1.06}$	1.7	0.6	..	$12.81^{0.18}_{0.18}$	3.90 ± 0.03	..	..	..
18174160-135628	MZM22	M0	1.11	$9.95^{0.38}_{-0.32}$	1.4	4.5	..	$13.63^{0.20}_{0.20}$	3.61 ± 0.02	..	..	..
18175212-171508	MZM23	M2	1.97	$13.39^{0.82}_{-1.15}$	..	-1.5	..	$13.34^{0.35}_{0.35}$	3.74 ± 0.03	..	..	..
18184453-165108	MZM25	M0	2.41	..	..	0.0	..	..	3.42 ± 0.02	..	..	..
18184660-163456	MZM26	M3	1.59	$12.98^{0.72}_{-1.11}$	1.4	1.2	..	$12.82^{0.36}_{0.36}$	3.48 ± 0.03	..	..	..
18210685-150340	MZM33	M0.5	1.21	$13.17^{1.21}_{-1.27}$	..	0.6	..	$13.50^{0.13}_{0.13}$	3.92 ± 0.03	0.09	..	..
18210846-153209	MZM34	M5	1.16	$12.18^{0.74}_{-0.83}$	1.5	1.2	..	$13.35^{0.18}_{0.18}$	3.77 ± 0.03	0.09	..	..
18212427-135528	MZM35	M0.5	1.00	$10.27^{0.44}_{-0.48}$	1.3	3.4	..	$13.56^{0.14}_{0.14}$	3.79 ± 0.02	..	..	..
18230411-135416	MZM37	M2	1.08	$13.25^{0.76}_{-0.72}$	1.4	0.4	..	$13.83^{0.14}_{0.14}$	3.62 ± 0.03	..	..	..
18231119-135758	MZM38	M1	1.21	$13.06^{0.64}_{-0.63}$	1.2	0.7	..	$13.76^{0.19}_{0.19}$	3.47 ± 0.03	..	..	..
18240991-110121	MZM39	K5.5	0.74	$11.52^{0.52}_{-0.57}$	1.3	2.8	..	..	3.91 ± 0.03	..	..	..
18251120-114056	MZM40	M2	0.77	$11.72^{0.47}_{-0.55}$	1.1	2.0	..	$13.51^{0.16}_{0.16}$	3.81 ± 0.02	0.15	0.52	..
18254382-115336	MZM41	M0	0.71	$13.80^{0.65}_{-0.62}$	0.9	1.2	$12.60^{0.21}_{-0.26}$	$13.64^{0.14}_{0.14}$	3.91 ± 0.03	..	..	..
18261922-140648	MZM42	M3	0.74	$13.97^{0.69}_{-0.80}$	1.1	-0.3	..	$13.41^{0.17}_{0.17}$	3.98 ± 0.03	0.09	..	..
18291233-121940	MZM45	M0	0.94	$12.77^{1.16}_{-0.66}$	1.3	1.2	$11.48^{0.46}_{-0.68}$	$13.12^{0.16}_{0.16}$	3.91 ± 0.02	..	..	..
18301889-102000	MZM46	M0	0.77	$14.21^{1.21}_{-1.01}$	..	-0.4	..	$13.25^{0.15}_{0.15}$	3.89 ± 0.03	0.07	0.33	215.37
18310460-105426	MZM47	M1	1.07	$13.94^{0.93}_{-1.11}$	1.4	0.2	..	$13.64^{0.14}_{0.14}$	3.87 ± 0.02	0.06	..	..
18315881-111921	MZM48	M0	0.96	$14.03^{0.80}_{-0.78}$	..	-0.6	..	$13.74^{0.17}_{0.17}$	3.73 ± 0.03	0.09	..	..
18334444-065947	MZM50	M1	0.85	$12.09^{0.57}_{-0.50}$	0.9	2.4	..	$13.65^{0.16}_{0.16}$	3.81 ± 0.02	0.09	0.59	..
18352902-072112	MZM54	M2.5	1.75	$13.89^{0.88}_{-1.16}$	1.3	0.4	..	$13.39^{0.16}_{0.16}$	3.80 ± 0.03	..	..	..
18353475-075648	MZM55	M0	1.60	$13.57^{0.79}_{-0.96}$	..	-0.5	..	$13.37^{0.18}_{0.18}$	3.52 ± 0.03	..	..	..
18354911-073443	MZM56	M1	1.48	$12.18^{1.21}_{-0.96}$	..	1.9	..	$13.06^{0.15}_{0.15}$	3.32 ± 0.03	..	..	..
18355151-073011	MZM57	M3.5	2.16	$13.73^{1.07}_{-1.63}$	1.3	0.2	..	$13.15^{0.16}_{0.16}$	2.61 ± 0.02	..	..	..
18374651-071224	MZM58	M1.5	1.71	$13.97^{1.03}_{-1.12}$	..	-0.6	..	..	3.91 ± 0.03	0.06	..	..
18413481-044857	MZM59	M1.5	1.05	$12.86^{1.00}_{-0.97}$	..	2.1	..	$13.48^{0.20}_{0.20}$	4.00 ± 0.03	..	..	..
18414834-044852	MZM60	M1.5	1.14	$13.25^{1.06}_{-0.87}$	1.9	0.4	..	$13.98^{0.18}_{0.18}$	3.99 ± 0.03	..	..	..
18421710-044116	MZM61	M1.5	2.59	..	..	0.0	..	..	3.38 ± 0.02	..	..	..
18424231-044053	MZM62	M3	0.90	$12.40^{0.70}_{-0.68}$	1.3	1.5	..	$13.51^{0.17}_{0.17}$	3.85 ± 0.03	..	0.29	109.56
18424479-043357	MZM63	M0.5	0.81	$13.30^{0.49}_{-0.55}$	1.1	0.8	$13.25^{0.14}_{-0.15}$	$13.50^{0.17}_{0.17}$	3.82 ± 0.03	..	..	..
18425222-034618	MZM64	M2.5	1.56	$12.66^{0.92}_{-1.02}$	1.4	0.5	..	$13.67^{0.32}_{0.32}$	3.68 ± 0.02	..	..	..
18430800-035624	MZM65	M2.5	2.30	..	..	0.0	..	..	4.04 ± 0.03	..	..	..
18442616-033527	MZM66	M0.5	1.35	$13.60^{0.86}_{-0.69}$	..	-1.1	..	$13.77^{0.16}_{0.16}$	3.72 ± 0.03	..	..	..
18464441-032404	MZM67	M4	1.68	$10.36^{0.75}_{-0.56}$	1.8	2.2	..	..	3.35 ± 0.02	..	..	..
18464480-030332	MZM68	M2	1.16	$13.58^{0.81}_{-0.70}$	..	-0.4	..	$13.32^{0.15}_{0.15}$	3.60 ± 0.02	..	..	..
18475357-014715	MZM69	M2	1.40	$13.79^{0.58}_{-0.81}$	..	-1.1	..	$13.38^{0.17}_{0.17}$	3.90 ± 0.03	..	..	..
18482997-021150	MZM70	M1.5	1.25	$13.08^{0.90}_{-0.87}$	1.6	0.2	..	$12.85^{0.18}_{0.18}$	3.55 ± 0.03	..	..	..
18543443+015304	MZM72	M1	2.03	$12.58^{1.06}_{-1.10}$	1.5	0.9	..	..	3.48 ± 0.03	..	..	..
18565849+013452	MZM74	M1	0.96	$12.64^{0.79}_{-0.66}$	1.1	1.2	$13.25^{0.19}_{-0.19}$	$13.94^{0.20}_{0.20}$	3.99 ± 0.03	..	..	..
18580434+021541	MZM75	M0.5	0.91	$13.09^{0.68}_{-0.82}$	1.2	1.2	$13.49^{0.22}_{-0.20}$	$14.05^{0.14}_{0.14}$	3.61 ± 0.03	..	0.17	183.80
19001228+031225	MZM77	M1	0.80	$11.72^{0.52}_{-0.43}$	1.3	2.5	$13.00^{0.21}_{-0.22}$	..	3.89 ± 0.02	..	0.10	189.12
19001812+032541	MZM78	M0.5	0.97	$12.92^{0.71}_{-0.67}$	2.0	0.4	..	$13.80^{0.25}_{0.25}$	3.77 ± 0.03	..	..	..
19060934+055844	MZM83	K5.5	0.74	$13.36^{0.86}_{-0.97}$	2.8	0.5	..	$13.53^{0.14}_{0.14}$	3.93 ± 0.02	0.06	0.48	148.50
19102566+081852	MZM84	M1	0.94	$13.07^{0.78}_{-0.76}$	1.8	0.1	..	$13.33^{0.16}_{0.16}$	3.95 ± 0.02	0.09	0.64	146.01
19125995+094801	MZM85	M7	0.61	$13.27^{1.10}_{-0.74}$	1.6	-0.0	..	$14.07^{0.18}_{0.18}$	3.92 ± 0.03	0.39	..	..
19130113+100159	MZM86	M1	0.87	$12.97^{0.75}_{-0.67}$	2.7	0.4	$13.89^{0.47}_{-0.60}$	$13.85^{0.15}_{0.15}$	3.88 ± 0.03	..	0.18	457.63
19141414+102802	MZM87	M2.5	1.06	$12.15^{0.69}_{-0.57}$	2.2	1.5	..	$14.63^{0.18}_{0.18}$	3.83 ± 0.02	..	..	..
19214456+133722	MZM91	M1.5	1.03	$12.89^{0.78}_{-0.76}$	1.3	1.0	..	$14.79^{0.22}_{0.22}$	3.96 ± 0.03	0.07	..	..

2MASS-ID: Source designation in the 2MASS catalog (Cutri et al. 2003).

MZM-ID: Source designation in the catalog of Messineo et al. (2016).

RSG-Sp: Spectral-type from Messineo et al. (2016).

A_{K_s}: extinction in K_s-band calculated as in Messineo et al. (2017) and Messineo & Brown (2019).

DM1: distance moduli from Messineo et al. (2017) (based on clump stars).

DM2: Gaia EDR3 parallactic distances from Bailer-Jones et al. (2021), as in Messineo & Brown (2021).

RUWE: Gaia EDR3 renormalized unit weight error (Gaia Collaboration et al. 2021).

frac: Gaia EDR3 ratio of the parallax values and their errors (Gaia Collaboration et al. 2021).

K_{so}: dereddened 2MASS K_s magnitudes, as in Messineo et al. (2017) and Messineo & Brown (2019).

Ampl(1): estimated Gaia amplitudes from the Gaia DR2 photometric uncertainty by Mowlavi et al. (2021). Ampl(2), Per(2): magnitude amplitudes and periods from the AAVSO International Variable Star database (VSX) (Watson et al. 2006a).

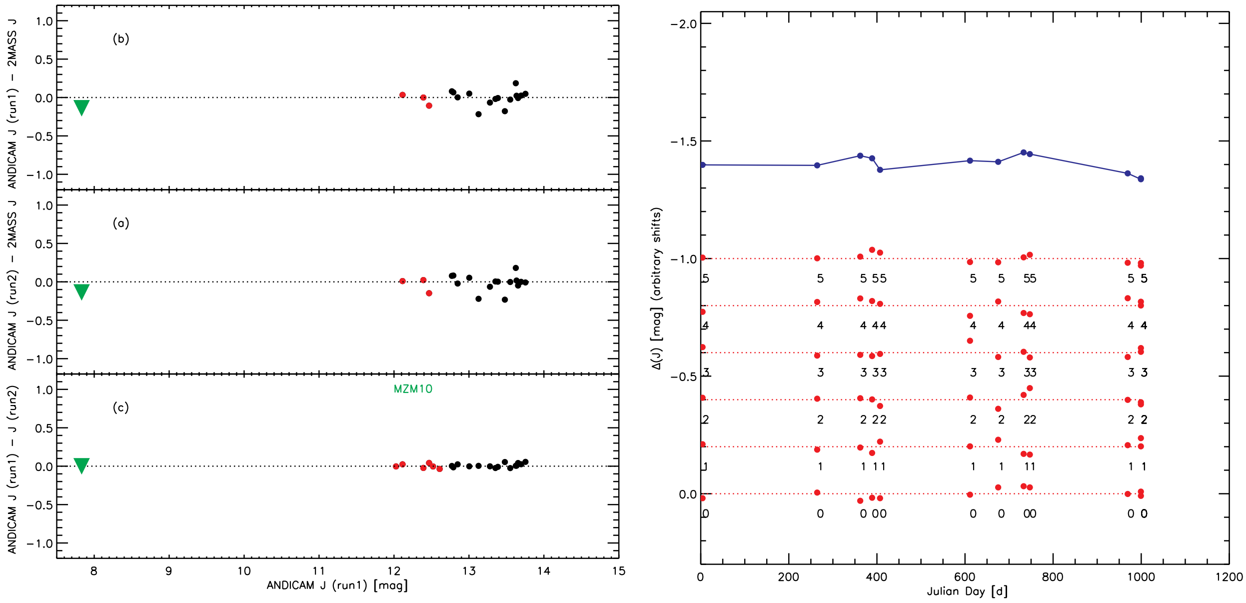

Fig. 2. *Left panel:* Diagram of the ANDICAM J magnitudes vs. the differences between the 2MASS and the ANDICAM J magnitudes (a and b) and between two ANDICAM epochs (c), in the field of MZM10. Red-filled circles mark stars used for the photometric calibration. The green triangle shows the location of MZM10. *Left panel:* Magnitude variations, Δ (J), in J-band vs. time of the MZM10 star (blue). The I-band variations of its photometric calibrators are also shown (red). The calibrators are stars taken from the same field of view (see text) and are marked with 0, 1, 2, 3, 4, and 5.

4 *J*-band observations

The infrared array of ANDICAM consists of 1024×1024 pixels (512×512 pixels with a pixel scale of $0\farcs276$ pix^{-1} after a default 2×2 binning) and has a field of view of $2\farcm4 \times 2\farcm4$. We used the J-filter. The observing sequence is made with the classical 7 dithered positions (the dither scale parameter was set to 40, i.e., each dithered position is within $20''$ from the center, or, equivalently, the center moves within a box of $40'' \times 40''$). Eight exposures were taken for each star. Each exposure consists of two coadds and their integration times ranged from 4 s to 30 s. This allowed us to obtain an excellent sky subtraction (using a robust mean with a 2 σ clipping). Each frame was sky-subtracted and flat-fielded.

The world coordinate system of each J-band exposure was created using, as a reference system, the coordinates of bright 2MASS J point sources ($J > 14$ mag) detected by ANDICAM.

The peaks of the stellar counts vary from a few hundred to 3,000, as recommended in the ANDICAM manual. A few frames were discarded because of saturation.

Typically, the FWHM of the PSF ranged from $1''$ to $1\farcs4$. Aperture photometry was performed using the DAOPHOT (Stetson 1987) version available in the NASA IDL Astronomy User's Library (Landsman 1993). Aperture photometry was performed on each frame (at each dithered position) as the targeted stars are among the brightest in the field and the derived magnitudes were averaged.

4.1 J-band flux calibration

Photometric calibration was performed in a relative manner. The measured magnitudes were registered on those measured in the first (reference) epoch. The absolute calibration was done using field stars with known 2MASS J-band magnitudes brighter than 13 mag. The calibrators were visually inspected and a few stars with a larger dispersion discarded (see Fig. 2). In a given field, the average standard deviation of the calibrator ANDICAM J magnitudes ranges from 0.001 to 0.044 mag, as listed **in** Table 2.

The average J-band magnitudes of the targets range from 6.9 to 11.6 mag, as listed in Table 2.

5 *I*-band observations

The ANDICAM CCD detector was also used for simultaneous I-band observations, taken in staring mode. The detector with 1024×1024 pixels covers a field of view of $6.'33 \times 6.'33$. For each observation, from 6 to 7 frames were acquired. The integration time was set to 8 s, and we reached a peak of 50 counts on a 16 mag star with a seeing of $1.''1$.

The CCD frames are distributed by the observatory after corrections for bias and flat field. The individual frames were combined with a 10 σ clipping.

For the astrometric calibration of each observation, DENIS data points brighter than I = 15 mag (or 13 mag in the denser field) were overlaid on the CCD image. The absolute astrometric solution is $\approx 0.''15$ accurate. For the 12 missing fields, 2MASS J-band data points were used.

Aperture photometry was performed using the daophot (Stetson 1987) version available in the NASA IDL Astronomy User's Library (astron). For each field, the full width half maximum (FWHM) was measured and the aperture radius set to FWHM*0.5+1.5 pix, and the sky annulus taken from FWHM*0.5+2 to FWHM*0.5+4 pix.

5.1 I-band flux calibration

The target magnitude calibration was done in a relative manner by using field stars with known flux; the absolute calibration only affects the global zero point, but not the magnitude variations.

For every epoch, the extracted catalog of point source was cross-correlated with that of the reference epoch (usually the first epoch), and flux calibrated. Most of the observed fields (57 minus 12) were covered by the DENIS survey (Epchtein et al. 1994). The DENIS observations in the Gunn-I filter saturate at around 10 mag and have a 3 σ detection limit at 19 mag, e.g., as described in Messineo et al. (2004), as shown in Fig. 3. Therefore, DENIS fully covers the range of interest, as the I magnitudes of the detected targets range from 10.8 to 17.5 mag. DENIS point sources with 10 <

Table 2. The average J and I magnitudes of the observed stars.

NAME	ANDICAM J						ANDICAM I								
	Nobs(J)	Ncal(J)	<std_cal(J)>	<mag$_*$(J)>	$\sigma_*(J)$	σ_{ext}	Nobs(I)	Ncal(I)	<std_cal(I)>	<mag$_*$(I)>	$\sigma_*(I)$	$<\sigma I_{circa}>$	σ_{ext}	$\Delta_{DEN-PAN}$ C$_A$	$\Delta_{DEN-VPHAS}$
			[mag]	[mag]	[mag]	[mag]			[mag]	[mag]	[mag]	[mag]	[mag]	[mag]	[mag]
18112728-175014	11	3	0.020	8.420	0.027	0.087	13	5	0.018	15.687	0.133	0.103	0.038	-0.084	0.003
18114736-192915	19	2	0.017	9.351	0.016	0.002									
18131562-180122	13	4	0.015	8.017	0.039	0.027	10	4	0.009	15.311	0.126	0.050	0.037	-0.116	-0.063
18132341-185818	12	8	0.024	8.851	0.038	0.057	10	5	0.025	15.054	0.051	0.045	0.023	-0.109	-0.046
18134914-184633	13	2	0.012	8.280	0.035	0.013	13	7	0.026	15.480	0.157	0.071	0.092	-0.157	-0.178
18140682-190620	12	6	0.024	7.830	0.039	0.073	12	8	0.028	15.043	0.118	0.053	0.064	-0.119	-0.046
18144593-173754	13	6	0.015	9.809	0.042	0.035									
18154112-164645	13	5	0.026	7.979	0.044	0.019	11	6	0.023	14.497	0.097	0.042	0.058	-0.151	-0.123
18155832-165827	34	5	0.028	9.219	0.034	0.022									
18171598-140554	12	4	0.024	7.340	0.021	0.039	12	5	0.017	13.232	0.052	0.021	0.073	-0.060	-0.084
18172865-163739	14	2	0.021	8.516	0.026	0.002	10	7	0.021	15.927	0.096	0.090	0.080	-0.122	-0.081
18174160-135628	7	3	0.026	7.650	0.029	0.044	11	6	0.031	14.187	0.119	0.037	0.106	-0.078	-0.060
18175212-171508	13	5	0.022	10.279	0.021	0.031									
18184453-165108	12	1	0.001	11.305	0.019	0.000									
18184660-163456	14	1	0.020	9.089	0.027	0.000	3	10	0.012	17.488	0.149	0.077	0.084	-0.048	-0.054
18210685-150340	14	1	0.007	8.126	0.045	0.000	13	9	0.015	15.322	0.157	0.135	0.044	-0.151	-0.152
18210846-153209	11	4	0.018	8.358	0.037	0.048	11	4	0.040	15.087	0.147	0.079	0.103	-0.210	-0.204
18212427-135528	12	9	0.030	7.515	0.027	0.032	12	6	0.026	13.587	0.101	0.082	0.047	-0.102	-0.081
18230411-135416	9	5	0.030	7.671	0.022	0.053	10	4	0.020	13.757	0.032	0.033	0.150	-0.121	-0.189
18231119-135758	13	2	0.030	7.826	0.033	0.029	11	4	0.021	14.337	0.060	0.084	0.059	-0.117	-0.157
18240991-110121	9	8	0.023	6.903	0.022	0.050	10	6	0.023	11.533	0.056	0.042	0.119	-0.152	-0.157
18251120-114056	10	4	0.032	7.036	0.043	0.065	12	6	0.017	12.690	0.209	0.022	0.097	-0.209	-0.188
18254382-115336	9	11	0.027	6.853	0.012	0.095	11	9	0.021	10.818	0.015	0.022	0.062	-0.224	-0.190
18261922-140648	12	3	0.027	7.485	0.099	0.113	12	27	0.023	13.689	0.158	0.032	0.043	-0.198	-0.196
18291233-121940	12	4	0.017	7.523	0.010	0.086	10	6	0.029	12.639	0.018	0.024	0.069	-0.160	-0.181
18301889-102000	11	6	0.020	6.975	0.026	0.073	10	5	0.028	11.865	0.087	0.045	0.116	-0.302	-0.256
18310460-105426	13	8	0.029	7.859	0.039	0.067	12	7	0.030	14.658	0.062	0.042	0.058	-0.224	-0.237
18315881-111921	12	2	0.024	7.308	0.036	0.028	12	8	0.012	13.561	0.063	0.023	0.027	-0.192	-0.160
18334444-065947	11	5	0.033	7.169	0.065	0.062	12	4	0.015	13.174	0.227	0.030	0.030	-0.166	-0.147
18352902-072112	13	2	0.006	9.929	0.030	0.011									
18353475-075648	55	5	0.025	9.118	0.031	0.038									
18354911-073443	13	6	0.024	8.686	0.067	0.034	8	7	0.016	16.157	0.084	0.089	0.058	-0.167	-0.160
18355151-073011	14	1	0.071	10.083	0.030	0.000									
18374651-071224	13	2	0.018	9.743	0.023	0.004									
18413481-044857	13	4	0.035	7.849	0.037	0.148	11	10	0.027	13.848	0.079	0.029	0.069	-0.254	-0.279
18414834-044852	12	2	0.024	8.180	0.023	0.010	11	11	0.028	14.571	0.063	0.034	0.076	-0.263	-0.316
18421710-044116	13	3	0.024	11.426	0.064	0.029									
18424231-044053	13	5	0.024	7.519	0.031	0.021	12	8	0.015	13.181	0.085	0.125	0.062	-0.171	-0.216
18424479-043357	12	4	0.034	7.105	0.030	0.059	11	13	0.021	11.983	0.039	0.024	0.050	-0.237	-0.239
18425222-034618	14	5	0.037	9.250	0.036	0.027									
18430800-035624	12	5	0.018	11.650	0.027	0.019									
18442616-033527	12	2	0.044	8.504	0.067	0.004	9	9	0.030	15.959	0.101	0.073	0.073	-0.283	-0.280
18464441-032404	15	4	0.027	9.321	0.027	0.071									
18464480-030332	10	2	0.026	7.875	0.031	0.007	11	2	0.014	14.333	0.032	0.033	0.115	-0.339	-0.293
18475357-014715	13	9	0.020	8.890	0.015	0.046	4	7	0.009	16.472	0.091	0.095	0.067	-0.379	-0.353
18482997-021150	14	2	0.044	8.039	0.036	0.034									
18543443+015304	14	1	0.000	10.299	0.046	0.000									
18565849+013452	9	8	0.030	7.667	0.017	0.593	12	4	0.016	12.887	0.025	0.020	0.018	-0.172	-0.183
18580434+021541	12	3	0.038	7.248	0.050	0.092	11	10	0.027	12.471	0.134	0.030	0.133		
19001228+031225	11	4	0.041	7.030	0.020	0.149	10	10	0.035	11.904	0.010	3.450	0.075		
19001812+032541	10	2	0.024	7.467	0.040	0.011	6	5	0.025	13.981	0.083	0.048	0.222		
19060934+055844	10	1	0.022	7.024	0.067	0.000	11	3	0.037	12.374	0.163	0.116	0.090		
19102566+081852	9	2	0.017	7.528	0.049	0.007	11	3	0.029	13.504	0.138	0.028	0.305		
19125995+094801	11	6	0.035	7.170	0.172	0.044	10	19	0.025	12.623	0.366	0.037	0.170		
19130113+100159	12	4	0.038	7.302	0.031	0.065	12	20	0.031	12.513	0.046	0.039	0.116		
19141414+102802	14	2	0.017	7.907	0.020	0.007	9	18	0.027	14.202	0.031	0.040	0.480		
19214456+133722	12	2	0.042	7.874	0.036	0.008	9	12	0.023	13.720	0.053	0.032	0.142		

Notes: Nobs(J) = number of used J-band observations; Ncal(J) = number of surrounding stars used for the photometric calibration; <std_cal(J)> = mean standard deviation of the calibrator magnitudes; <mag$_*$(J)> = J-band average magnitude of the target; $\sigma_*(J)$ = standard deviation of the target magnitudes; σ_{ext} = the standard deviation of the differences between the ANDICAM J magnitudes (reference epoch) and the 2MASS J magnitudes of the calibrator stars; Nobs(I) = number of used J-band observations; Ncal(I) = number of surrounding stars used for the photometric calibration; <std_cal(I)> = mean standard deviation of the calibrator magnitudes; <mag$_*$(I)> = I-band average magnitude of the target; $\sigma_*(I)$ = standard deviation of the target magnitudes; $<\sigma I_{circa}>$ = mean of the standard deviations of field stars with magnitudes similar to that of the targeted late-type star; σ_{ext} = the standard deviation of the differences between the ANDICAM I magnitudes (reference epoch) and the I magnitudes from the external catalogs (DENIS or PANSTARRS). $\Delta_{DEN-PAN}$= median of (DENIS $I-$ PANSTARRS $I_{\rm AB}$ + 0.445) of field stars with $I < 17.0$ mag. $\Delta_{DEN-VPHAS}$ = median of (DENIS $I-$ VPHAS $I_{\rm Vega}$) of field stars with $I < 17.0$ mag.

Table 3. Magnitude variations in I- and J-bands of the targeted stars.

2MASS-ID	MZM	ANDICAM J(max)−J(min) [mag]	ANDICAM <J> − 2MASS J [mag] [d]	ANDICAM I(max) − I(min) [mag] [%]	ANDICAM <I> − DENIS I [mag] [mag]	fl_corr	fl_var	Period [d]	fap	ΔI/2 [mag]
18131562-180122	MZM06	0.127	−0.157	0.378	0.284	1	1	248	23	0.191
18134914-184633	MZM09	0.123	−0.103	0.453	0.567	1	1	433	11	0.167
18210685-150340	MZM33	0.182	−0.260	0.567	0.164	1	1	201	24	0.195
18210846-153209	MZM34	0.116	−0.045	0.487	0.151	1	1	167	6	0.184
18251120-114056	MZM40	0.109	−0.025	0.578	−0.065	1	1	432	13	0.215
18334444-065947	MZM50	0.190	−0.069	0.692	0.246	1	1	431	23	0.218
19060934+055844	MZM83	0.236	−0.006	0.530		1	1	279	43	0.166
19125995+094801	MZM85	0.517	0.067	1.076		1	1	260	23	0.453

ANDICAM J(max)−J(min) is the difference between the maximum and minimum ANDICAM J magnitudes.

ANDICAM $< J >$ − 2MASS J is the difference between the average ANDICAM J and the 2MASS J magnitudes.

ANDICAM I(max)−I(min) is the difference between the maximum and minimum ANDICAM I magnitudes.

ANDICAM $< I >$ − DENIS I is the difference between the average ANDICAM I and the DENIS I magnitudes.

fl_corr =1 if the Pearson correlation coefficient of the simultaneously taken I mag and J mag vectors is larger than 0.5.

fl_var =1 if the standard deviation of the I mag vector exceeds twice that of field stars at similar magnitudes or if the standard deviation of the J mag vector exceeds 2 times that of other bright field stars (non-variable calibrators).

Period of the periodic light variation detected in the Lomb-Scargle peridiogram (see text).

fap is the false alarm probability corresponding to the power level of the adopted period.

ΔI/2 is the semi-amplitude of the photometric I-band light-curve.

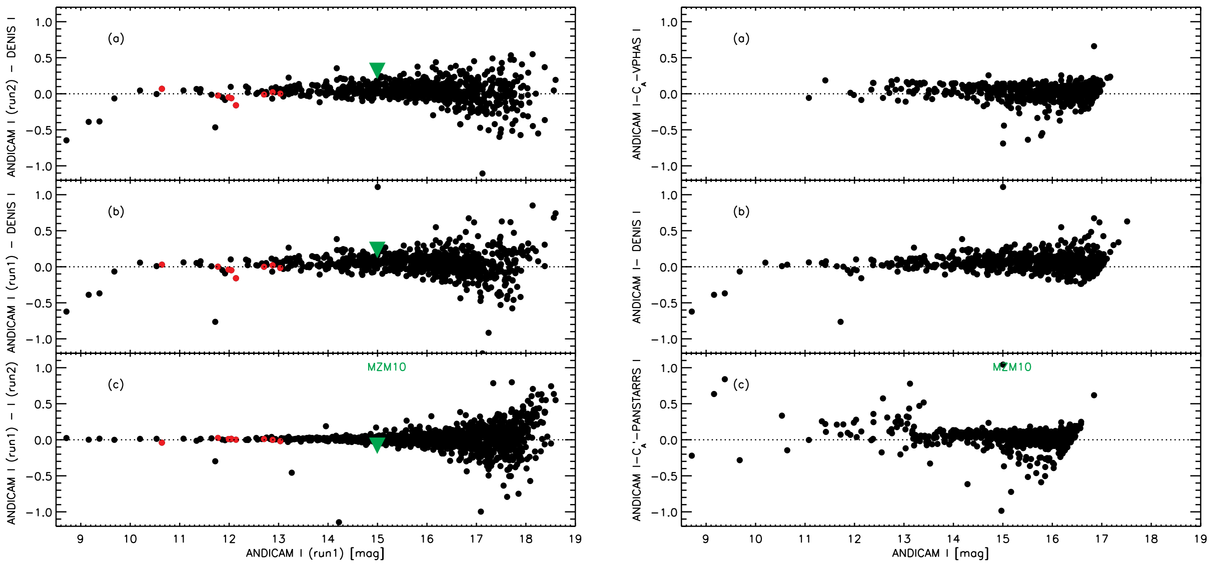

Fig. 3. *Right panel:* The differences between the DENIS and the ANDICAM I magnitudes (a and b) and between two ANDICAM epochs (c) are plotted vs. the ANDICAM I magnitudes. Red-filled circles mark stars used for the photometric calibration. The green triangle shows the location of MZM21. *Left panel:* For the first epoch of field MZM21, ANDICAM magnitudes are compared with VPHAS (a), DENIS (b), and PANSTARRS (c) magnitudes. The constant C_A values are as specified in Table 2 and and $C_{A'} = C_A - 0.445$.

I-mag < 13 mag were used to determine the night zero point; the median of the differences between the instrumental magnitudes and the DENIS I-mag was adopted.

ANDICAM mounts a KPNO-I filter, while the DENIS survey made use of a Gunn-I filter, as shown in Fig. 4. The average difference between the I-band magnitudes of the standard stars by Landolt (2009) in the Johnson-Kron-Cousins system and the DENIS I-band magnitudes is 0.015 mag with σ = 0.045 mag. This offset was not applied.

The average difference between the I-band magnitudes by Landolt (2009) and the SDSS I-

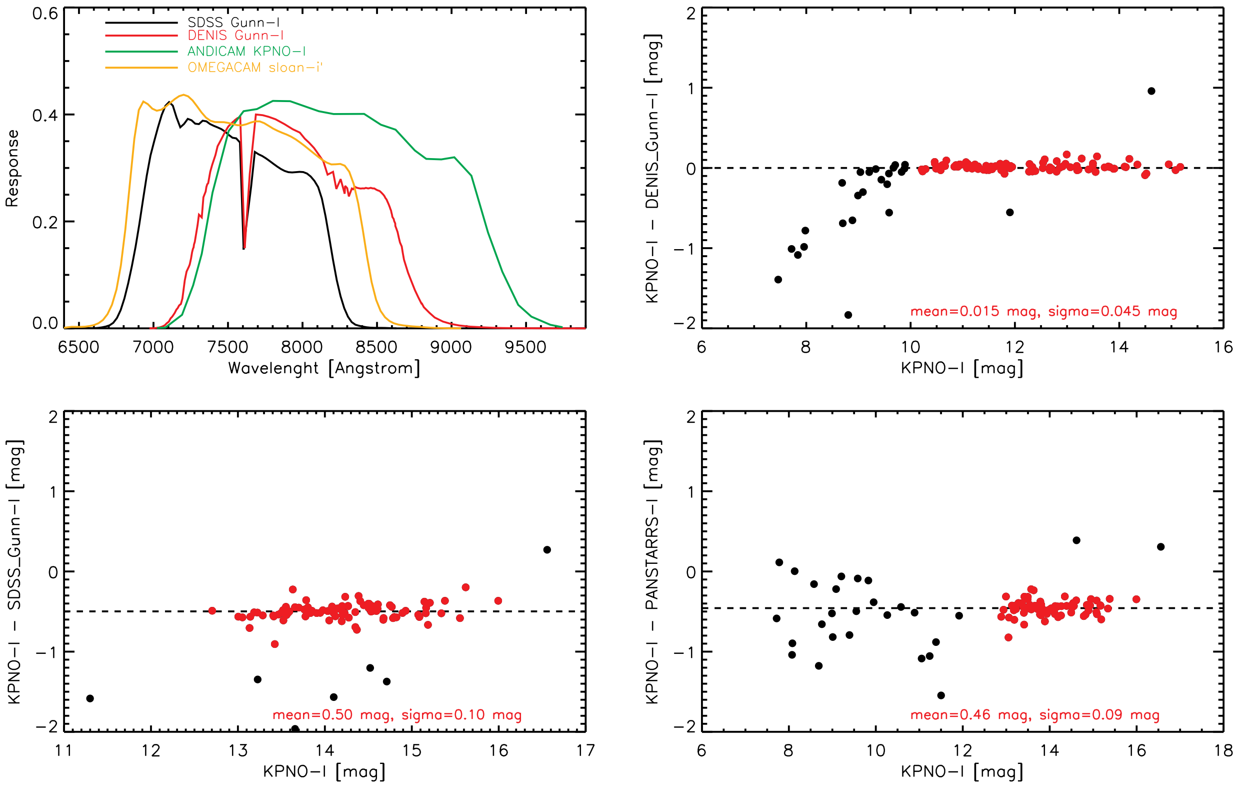

Fig. 4. The *left upper panel* displays the ANDICAM KPNO-I filter response in green, that of the DENIS Gunn-I filter in red, that of the SDSS Gunn-I filter in black, and that of the VPHAS sloan-i' in orange. In the *right upper panel*, the differences between the I-band magnitudes of the standard stars by Landolt (2009) (in the Johnson-Kron-Cousins system) and the DENIS I-band magnitudes are plotted. In the *right lower panel*, there are the differences between the I-band magnitudes by Landolt (2009) (in the Johnson-Kron-Cousins system) and the SDSS I-band magnitudes, and in the *left lower panel*, the differences between the I-band magnitudes by Landolt's system and the PANSTARRS I-band magnitudes.

band magnitudes is 0.50 mag with σ = 0.10 mag when 16< I-band < 13 mag. But, unfortunately, only 3 target fields were covered by the SDSS survey DR12 (Alam et al. 2015). The average difference between the I-band magnitudes by Landolt (2009) and the PANSTARRS I-band magnitudes (Mean PSF AB) from 16 to 13 mag is 0.46 with σ = 0.09 mag. The standard stars by Landolt (2009) are not covered by the Galactic Plane VPHAS+ survey (Drew et al. 2014). However, for most of the observed fields, I magnitudes are available from the VPHAS+, and average shifts from 0 to 0.3 mag are measured between the DENIS and VPHAS+ I (Vega system) magnitudes. The bright tail of stars detected in ANDICAM were saturated in PANSTARRS, and VPHAS+ I-band catalogs.

The absolute photometric calibration was refined by analyzing the time behaviours of field stars with DENIS 13 < I < 10 mag, and retaining as calibrators those stars with smaller ANDICAM time variations (std_cal(I)$_j$), i.e., with std_cal(I)$_j$ values within the field mean <std_cal(I)> plus 1.5 times their dispersion; std_cal(I)$_j$ varies from 0.013 mag to 0.048 mag.

For 12 fields calibrated with PANSTARRS (because not covered by DENIS), stars from 15.5 < I < 13 mag were used. An example of adopted calibrators is illustrated in Fig. 5. The computed average I-band magnitudes of the targets are listed in Table 2, along with some parameters (e.g., internal standard deviations of calibrator magnitudes, and external standard deviations of field stars detected in I-band by ANDICAM as well as by the DENIS, VPHAS+, and PANSTARRS surveys) to illustrate the uncertainties on the absolute calibration.

Only fields where the targeted stars were detected in at least 2 epochs were further analyzed (15 stars were below the detection threshold).

6 J-band and I-band variations

In order to assess the existence of significant variations in the brightness of the targeted stars, the σ of the target J magnitudes, $\sigma_*(J)$, are compared with the σ of the calibrator stars; indeed, the targets are among the brightest stars detected in J-band. In the I-band, the targets are faint; therefore, a σI_{circa} is calculated with field stars at the target I magnitude, and compared with $\sigma_*(I)$.

In the J-band analysis, four targets (MZM42, MZM56, and MZM85) have $\sigma_*(J)$ values larger than 3.5 times the <std_cal(J)> of their calibrators; this calculation permits the detections of variations larger than 0.07 mag, because the mean of the variations of the calibrators is 0.025 mag. In the I-band data, six stars appear significantly variable ($> 3.5 < \sigma I_{circa} >$) (MZM40, MZM42, MZM50, MZM75, MZM84, and MZM85). The mean σI_{circa} is 0.13 mag.

Despite the small numbers of detected variables, correlated trends appear in several I-band and J-band light-curves, as shown in Figs. 6 and 7. Sixteen targets (out of the 42 detected in both bands) have a Pearson correlation coefficient between I-band and J-band measurements above 50%, and the $\sigma_*(I)$ or $\sigma_*(J)$ of their I-band or J-band measurements is larger than twice the σ of corresponding field stars with similar magnitudes (<std_cal(J)> or $< \sigma I_{circa} >$). In this latter calculation, 38% of the sample shows variations, MZM06, MZM09, MZM10, MZM16, MZM20, MZM22, MZM33, MZM34, MZM40, MZM42, MZM50, MZM59, MZM75, MZM83, MZM84, and MZM85.
The use of multi-wavelength data improves the detection of variables and the correlated patterns make it more solid and reliable. When using combined IJ-bands, the variable detection threshold in a single band is lowered (from 3.5 σ to 2 σ) to detect more variables.

The Gaia variables listed by Mowlavi et al. (2021) were detected with a detection thresholds of 0.06 mag in G-band. It appears that variables with amplitudes in G-band larger than 0.08 mag are all retrieved. There are eight ANDICAM variables with estimated G variations below the 0.06 mag threshold for variability. While the Gaia variables retrieved by ANDICAM have average amplitudes in I-band of 0.27 mag (0.10 mag in J-band) and are mostly > 0.21 mag, variables found by ANDICAM,

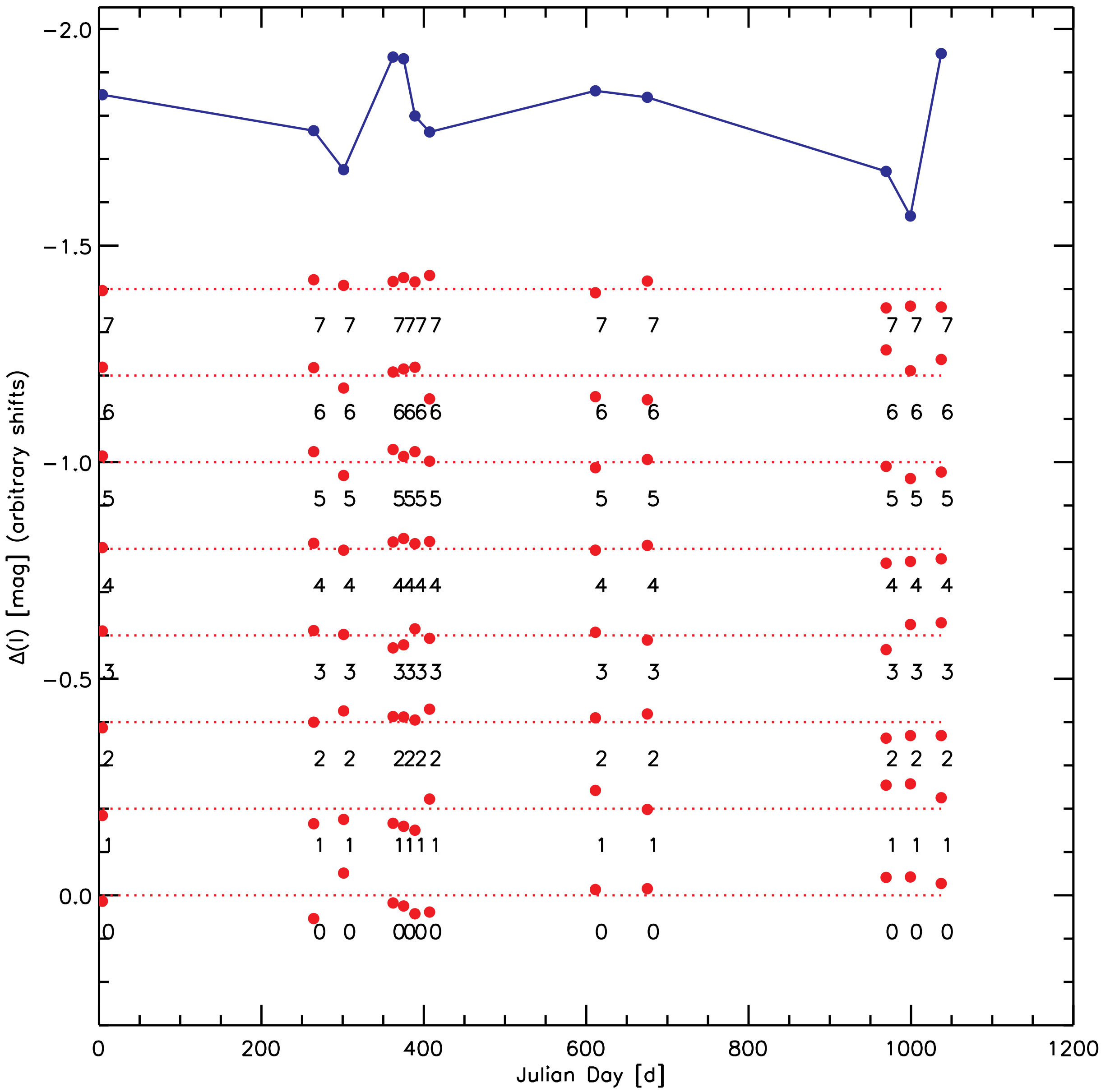

Fig. 5. Magnitude variations, Δ (I), in I-band vs. time of the MZM10 star (blue). The I-band variations of its photometric calibrators are also shown (red). The calibrators are stars taken from the same field of view (see text) and are marked with 0, 1, 2, 3, 4, 5, 6, and 7.

but not in Mowlavi et al. (2021), have average I-band amplitudes of 0.16 mag (0.09 in J-band) and are mostly < 0.21 mag. We conclude that the detection of variables is complete for I-band amplitudes larger than 0.21 mag.

While G-band amplitudes are determined for stars with a wide range of G-band (from 10 to 20 magnitudes), the variables reported in AAVSO are brighter than G-mag 14.5 mag.

A number of 24 (out of 42) stars, 57% of the sample, have J and I variations below the adopted detection threshold (2 σ).

The standard deviations of the targets and calibrators are listed in Table 2.

6.1 Peridiograms

Periods are obtained as the highest power in the Lomb-Scargle periodogram, which is an elaborated version of the classical peridiogram for unevenly sampled data (Horne & Baliunas 1986; Scargle 1982). The scargle.pro routine in the NASA IDL Astronomy Users Library was used (Landsman 1993). The analysis of the I-band Lomb-Scargle peridiogram yields periods for 8 stars (out of the 16 variables in Sect. 6), which are listed in Table 3. Only periods with power levels corresponding to false alarm probabilities (the probability for the periods to be false) below 50% were considered. The power of MZM83 corresponds to a false alarm probability (FAP) of 43.6%, while the probability remains below 25% for the other 7 stars. Their periods range from 167.6 to 433.3 days.

A higher FAP brings a better census of variables; however, it may bring false cases. A FAP value of 10% is commonly used in time-series photometry, as mentioned in the work of VanderPlas (2018). FAP values of 50% are also found in literature, for example in the spectroscopic time-series analysis of Cincunegui et al. (2007). Besides the Scargle method, a fitting of the light curve was performed and the sinusoidal curves are evident.

The 8 periodograms and phased light-curves are shown in Appendix. In conclusion, 38% of the 42 targets with ANDICAM IJ detections are found to be variable, and 19% show periodicity.

6.2 Amplitudes of the variations

16 late-type stars (out of 42 detected in both IJ bands) appear to have significant light variations when compared with surrounding field stars, as described in Sect. 6. The measured variations range from 0.038 mag to 1.076 mag in I-band, and from 0.031 to 0.517 mag in J-band, and are listed in Table 2. As mentioned in Sect. 6, the variations in I and J bands appear correlated. For pairs of simultaneously taken I and J magnitudes of the 16 variables, the I variations, ΔI, are plotted against the J variations, ΔJ, in Fig. 6. The ΔI values are 2.2 ± 0.1 times larger than the ΔJ values, and 1.292 ± 0.004 larger

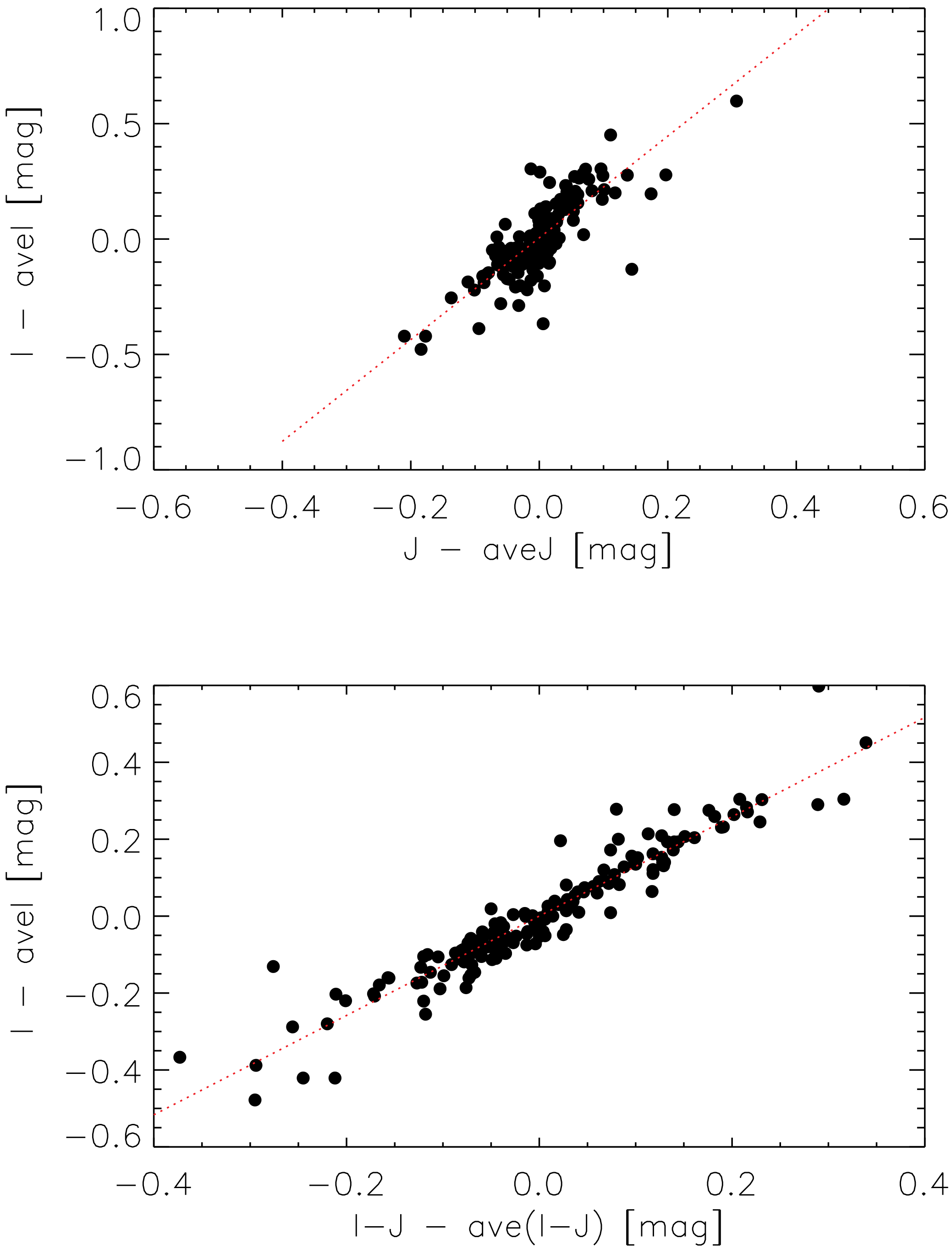

Fig. 6. *Top panel:* Variations in I-band vs. those simultaneously measured in J-band; all epochs of targets with detected variability are shown. In red a linear fit to the data. *Bottom panel:* Variations of I magnitudes vs. those measured in the $I-J$ colour. In red a linear fit to the data.

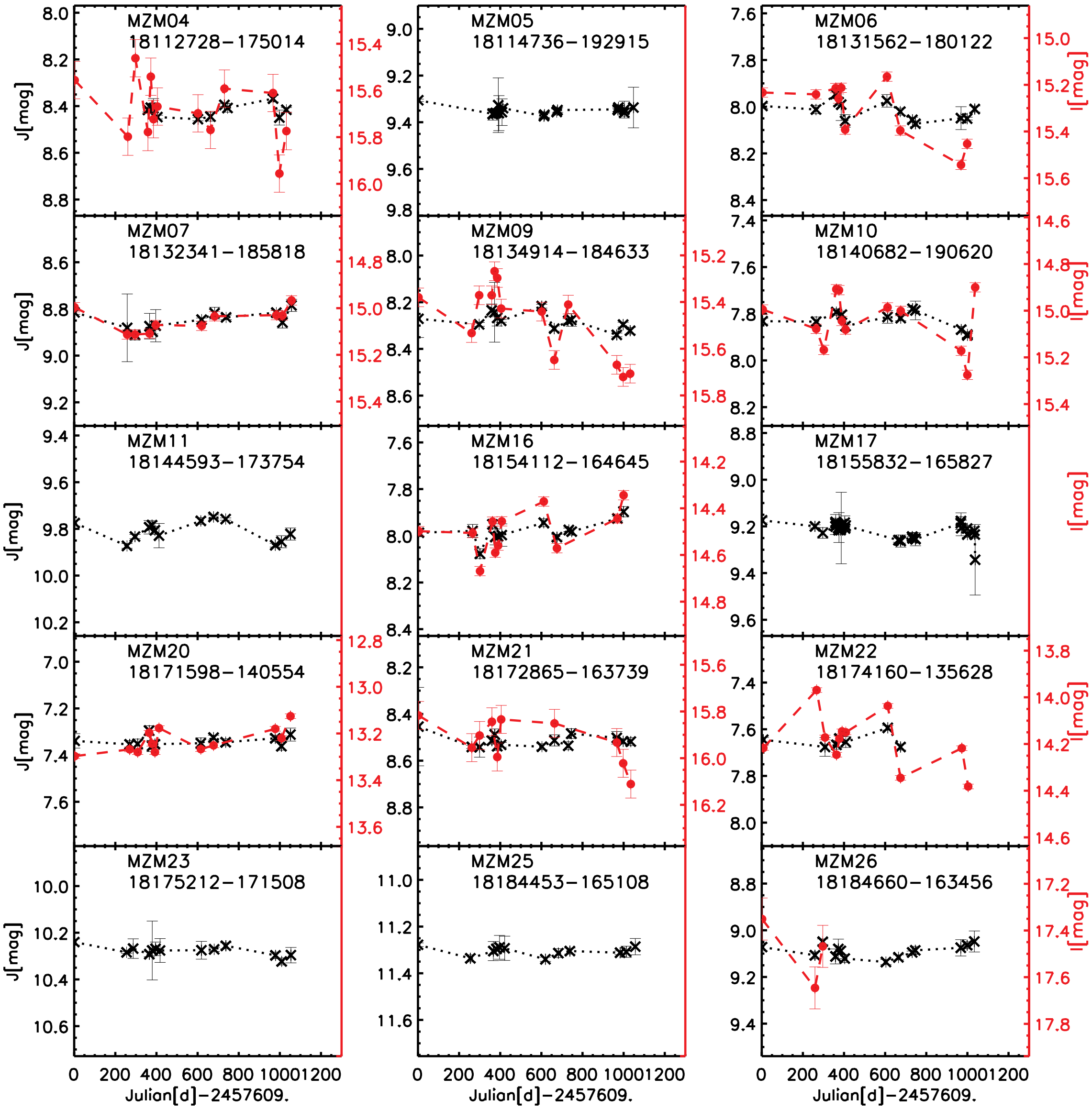

Fig. 7. In each panel, on the left y-axis, the J-band magnitudes vs. Julian days of one observed star are plotted with black X. Dotted-black lines connect the X points. The I-band magnitudes are over-plotted with red-filled circles and their values annotated on the right y-axis. Long-dashed red lines connect the circles. Two horizontal dotted-dashed lines are drawn at ± 0.15 mag distance from the average magnitudes of the observed star.

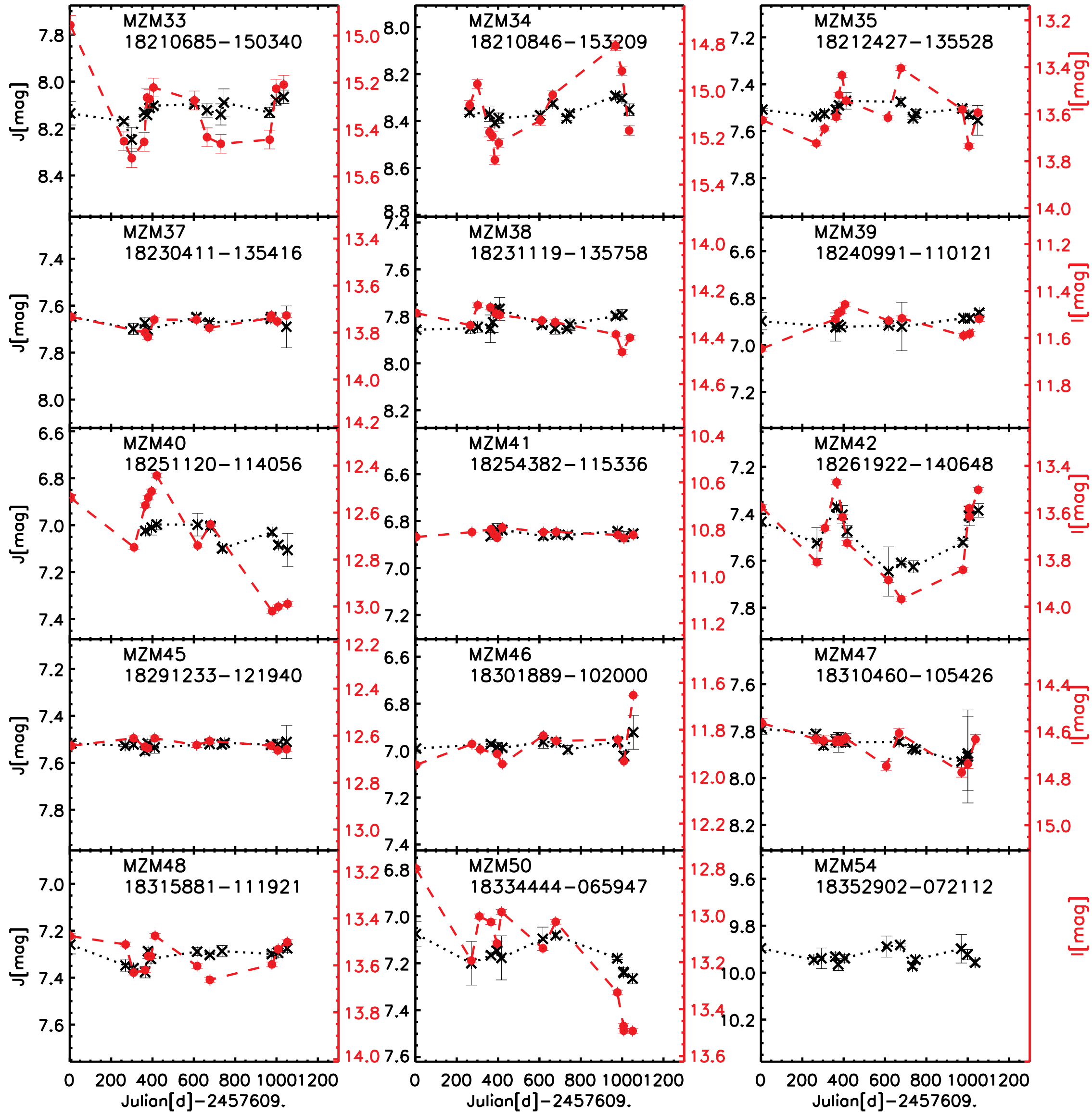

Fig. 7. Continuation of Fig. 7.

than those in the $I-J$ colors, $\Delta(I-J)$.

For the eight stars found to be periodic variables, the least-squares fitting of data by sinusoidal curves of the type $\mathrm{I(t)} = \frac{\Delta \mathrm{I}}{2} sin[2\pi(\frac{\mathrm{t}}{\mathrm{Per}} + \omega_{\mathrm{o}})] + < \mathrm{I} >$ was performed. For each curve, three parameters were estimated; $\frac{\Delta I}{2}$ is the semi-amplitude of the pulsation (i.e., the difference in absolute value between the mean value and the minimum or maximum deviation), ω_o is the value at zero phase (at the maximum), and $< I >$ is the mean magnitude of the pulsator. The $\frac{\Delta I}{2}$ values are listed in Table 3, and shown in Appendix.

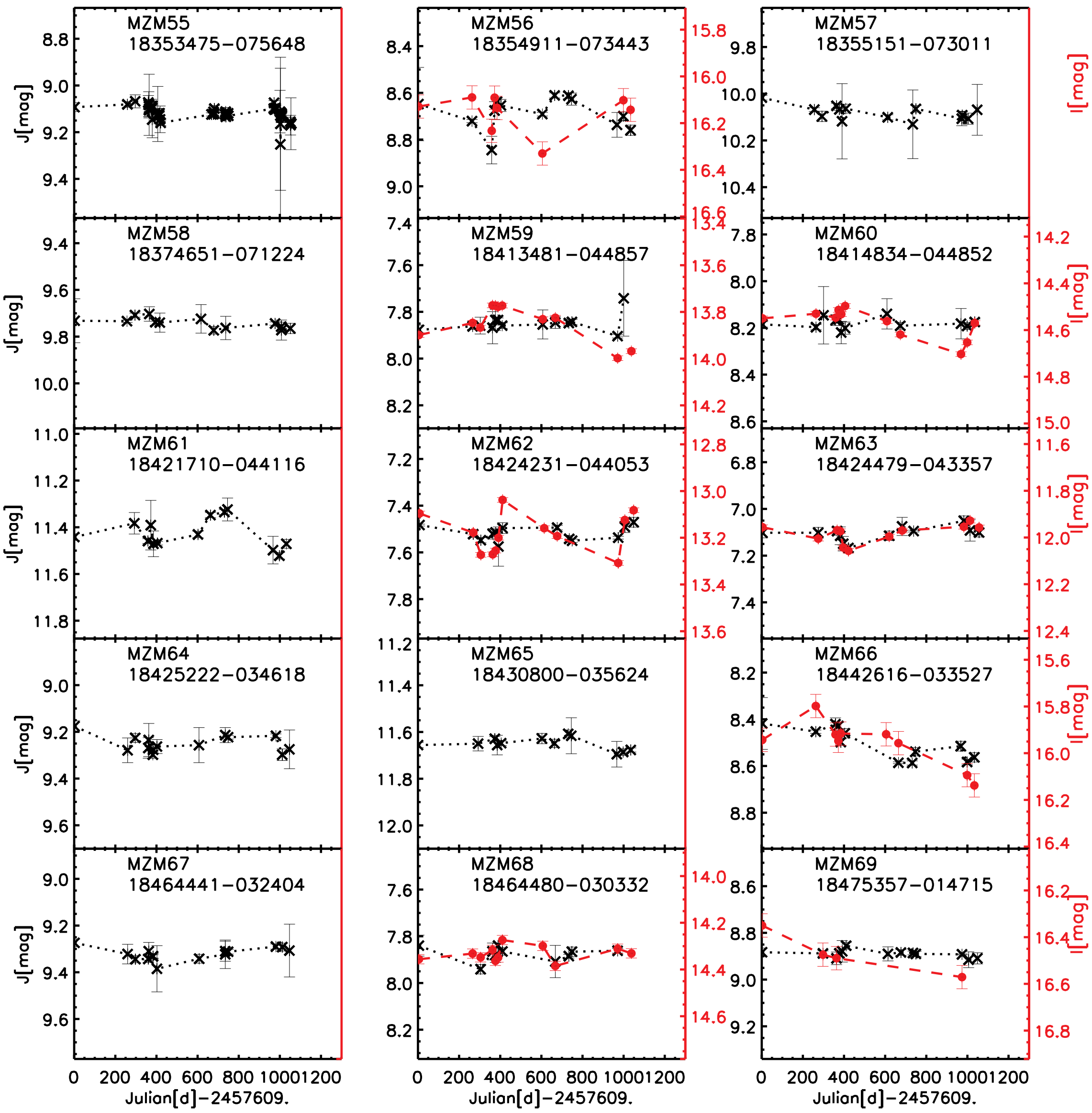

Fig. 7. Continuation of Fig. 7.

224 ## 7 Previously known variables

225 For nine targets, amplitudes are reported in the AAVSO International Variable Star database (VSX)
226 (Watson et al. 2006a), 4 of which were not detected as significantly varying in this work. They range
227 from 0.10 mag to 0.64 mag.

228 In the work of Mowlavi et al. (2021), there are estimates of G-band amplitudes for 15 of the
229 ANDICAM targets (10 of which were classified as a variable in this work); they are based on the
230 G-band photometric errors and range from 0.06 mag to 0.39 mag. These stars are not listed in the
231 GAIA DR2 table of long-period variables (LPV). This brings to 59% the fraction of variable targets
232 and known amplitudes.

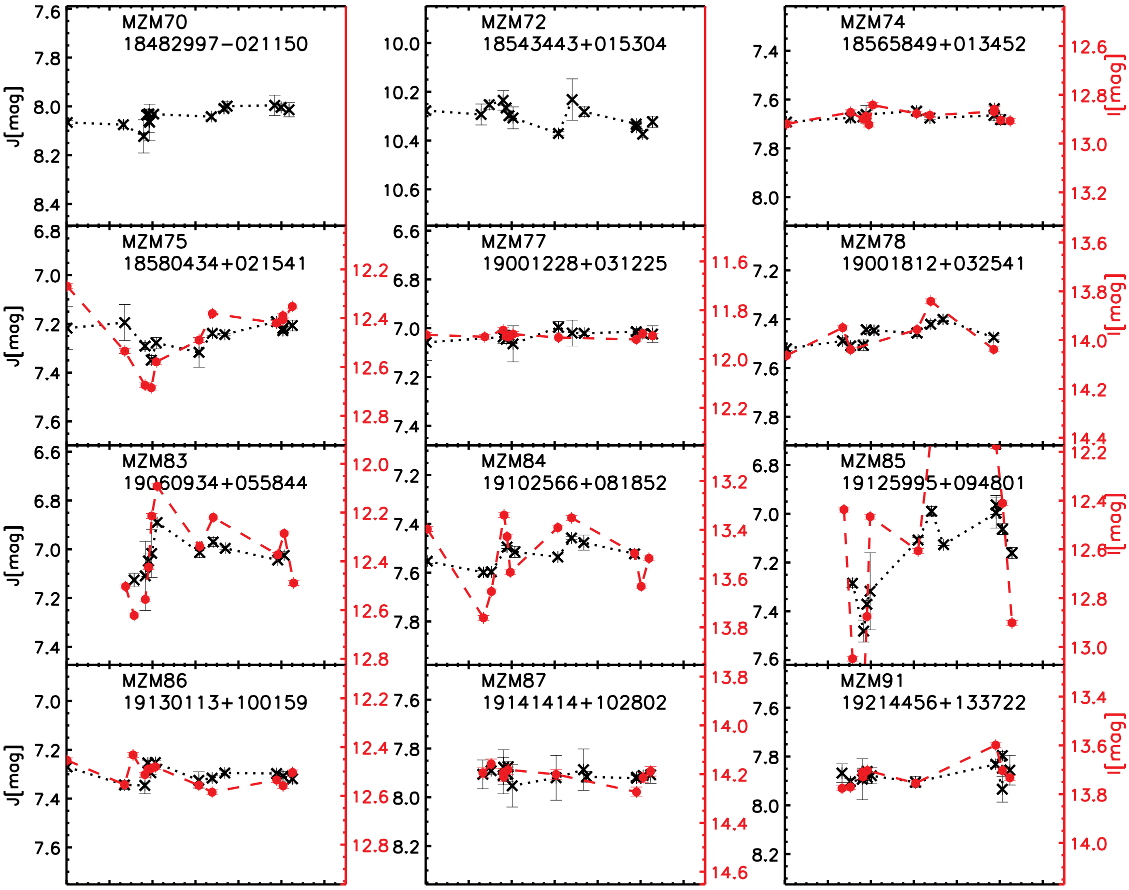

Fig. 7. Continuation of Fig. 7.

For seven targets, periods from 109 to 457 d are listed in the International Variable Star Index VSX (Watson et al. 2006b), four of which are not detected as significantly varying in this work. MZM83 has a period of 148.5 d in the AAVSO catalog, in the ANDICAM data a low power peak appears at 279 d with a high probability of 43% to be false. The other six AAVSO stars have no periods detected in ANDICAM.

This increases from 19% to 33% the number of targets with known periods.

8 M_K versus periods of known Galactic RSGs

To verify the newly obtained periods, the M_K versus period diagram of the targets is compared with that of well-studied variable RSGs in Fig. 8. For known variables, the periods are taken from Chatys et al. (2019) and the M_K values are those calculated by Messineo & Brown (2021) with EDR3 Gaia distances and are obtained as described in Messineo & Brown (2019). The distances adopted are based on EDR3 Gaia parallaxes and are the geometric distances by Bailer-Jones et al. (2021). The short periods ($< 2,000$ d) appear to describe a clear sequence in this plane. The sequence appears much improved with the use of EDR3 Gaia distances, and has a $\sigma = 0.32$ mag. The sequence is consistent with the fit made for RSGs in Perseus OB1 by Pierce et al. (2000), as well as with the fit obtained for RSGs in M31 by Soraisam et al. (2018).

At this stage, in the M_K-Period plane, the distribution of the 14 ANDICAM targets with determined periods appears consistent with that of known RSGs, within errors.

9 Summary and remarks

ANDICAM observations of a sample of late-type stars were obtained over a 1,054 day time period (2.9 years). Fifty-seven bright late-type targets from the sample of Messineo et al. (2017) were observed in J bands and 42 were detected in the simultaneously taken I band images. It appears that at least 38% of the ANDICAM sample is made of variable stars, 47% when including additional information in AAVSO, or 59% when considering also the Gaia amplitude estimates reported by Mowlavi et al. (2021). 19% have detected periodic behaviours in the ANDICAM data and 33% when including the AAVSO periods.

The targeted late-type stars have average ANDICAM $< J >$ from 6.85 to 11.65 mag and ANDICAM $< I >$ from 10.82 to 17.49 mag. However, despite their faintness in I-band, I-band is more suitable than J-band for detecting variables. Indeed, the magnitude variations measured in I-band are correlated with those seen in J-band and are a factor 2.2 larger. In I-band, the differences between the minimum and the maximum magnitudes of each star range from 0.04 to 1.08 mag, while in J-band from 0.03 mag to 0.52 mag.

The ANDICAM data here presented indicates that the I magnitudes and $I - J$ colors of the targets are varying in a correlated manner and that $\Delta I \propto 1.29\Delta(I - J)$. In pulsating large amplitudes stars, the amplitudes are known to decrease with increasing wavelength, as the envelope expands and cools down every radial pulse (Reid & Goldston 2002). For example, in Mira stars the V-band amplitudes can be even 8 mag (Reid & Goldston 2002), and the J-band amplitudes are about 1.6 times larger than those measured in K_s-band (Messineo et al. 2004). This effect is caused by a changing opacity in the

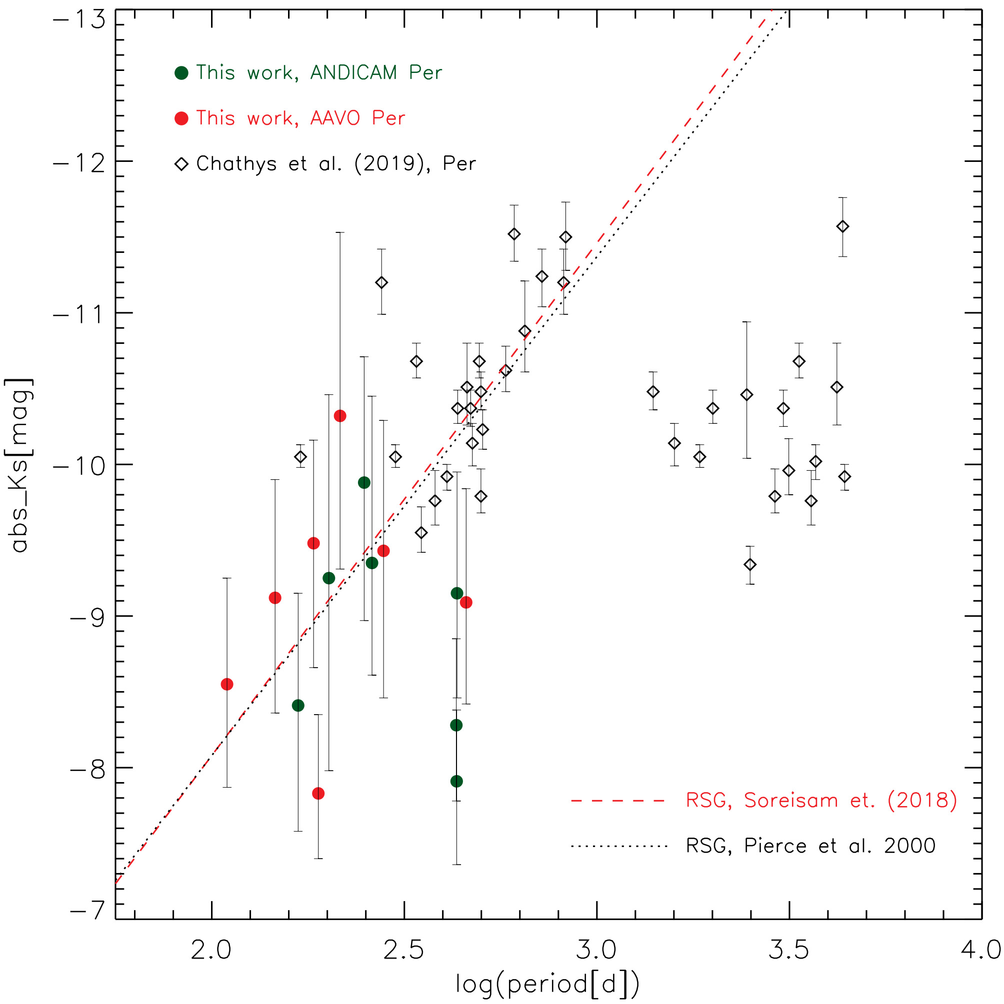

Fig. 8. M_K values vs. periods of Galactic RSGs (black diamonds). RSG periods are from Chatys et al. (2019) and M_K magnitudes based on Gaia EDR3 distance are from Messineo & Brown (2019) and Messineo & Brown (2021). Late-type from this work are overplotted marked with filled circles in red when the periods are taken from the AAVSO catalog and in dark-green when the periods are determined with ANDICAM data. The distances are from Gaia EDR3 Messineo & Brown (2021).

stellar atmosphere (Reid & Goldston 2002), due to molecular bands. When the late-type star pulses, it expands and cools down, and it reaches its minimum light when the atmospheric opacity is at the maximum value (Reid & Goldston 2002). When the long-period variable pulses, it cyclically changes its spectral type. As mentioned by Pierce et al. (2000), for RSGs the measured light variations are found to be a function of the used filter. The I-band spectrum is dominated by TiO molecular bands which are extremely sensitive to temperature variations, while the J-band spectrum is not affected by TiO bands. The observed correlation between the ANDICAM color variations, $\Delta(I-J)$, and the magnitude variations are, therefore, consistent with the expected behaviour for radial pulsation. For normal (static) giants and RSGs, a change of spectral type from M2 to M5 (M3.5 ±1.5) corresponds to a color change $\Delta(I-J) \approx 0.26$ mag (Johnson 1966). Variable RSGs could have larger color changes, due to their larger radii and the large convective cells present in their turbulent atmospheres.

As shown by Kiss et al. (2006) and Chatys et al. (2019), variable RSGs are of late-type (M-type). A broad correlation is found between the stellar luminosity and the *R*-band amplitudes of 120 RSGs (Soraisam et al. 2018). In turn, as average stellar temperatures decrease with increasing luminosity, a positive correlation also exists between the stellar temperatures and amplitudes (Messineo & Brown 2019, 2020). The sample here analyzed is small and no clear trend is observed between the luminosity and amplitudes. However, the small amplitudes are in agreement with supergiant classification. Indeed, the most luminous AGB stars (e.g., super-AGBs) are expected to be large-amplitude pulsators (O'Grady et al. 2021).

New periods are determined for eight late-type stars and range from 167 to 433 d, and seven periods are available from AAVSO. The time baseline of the ANDICAM data does not allow us to check for long secondary periods (LSP), which are typically longer than 2,000 d. In the Galaxy, LSP periods are seen in 50% of the RSGs (Chatys et al. 2019; Kiss et al. 2006).

The sample does not contain large-amplitude variables, which are bright luminous AGBs. For the targets found to be periodic variables, their distribution in the period-luminosity diagram suggests that they are RSGs, consistently with the work of Messineo et al. (2017). However, distance errors are still large and it is better to re-check with the final Gaia parallaxes. Gaia will also release spectra and G-band light-curves.

Due to the significant uncertainties in their distances, time-series measurements appear to offer a promising means of assessing the stellar luminosity class of obscured inner Galactic objects.

Appendix 1 Phased light-curves

In Fig. 9, the phased light-curves are shown. Periods are estimated for eight variables.

References

Alam, S., Albareti, F. D., Allende Prieto, C., et al. 2015, ApJS, 219, 12

Bailer-Jones, C. A. L., Rybizki, J., Fouesneau, M., Demleitner, M., & Andrae, R. 2021, AJ, 161, 147

Chatys, F. W., Bedding, T. R., Murphy, S. J., et al. 2019, MNRAS, 487, 4832

Cincunegui, C., Díaz, R. F., & Mauas, P. J. D. 2007, A&A, 461, 1107

Cutri, R. M., Skrutskie, M. F., van Dyk, S., et al. 2003, 2MASS All Sky Catalog of point sources.

de Jong, R. S., Bellido-Tirado, O., Chiappini, C., et al. 2012, in Society of Photo-Optical Instrumentation Engineers (SPIE) Conference Series, Vol. 8446, Ground-based and Airborne Instrumentation for Astronomy IV, ed. I. S. McLean, S. K. Ramsay, & H. Takami, 84460T

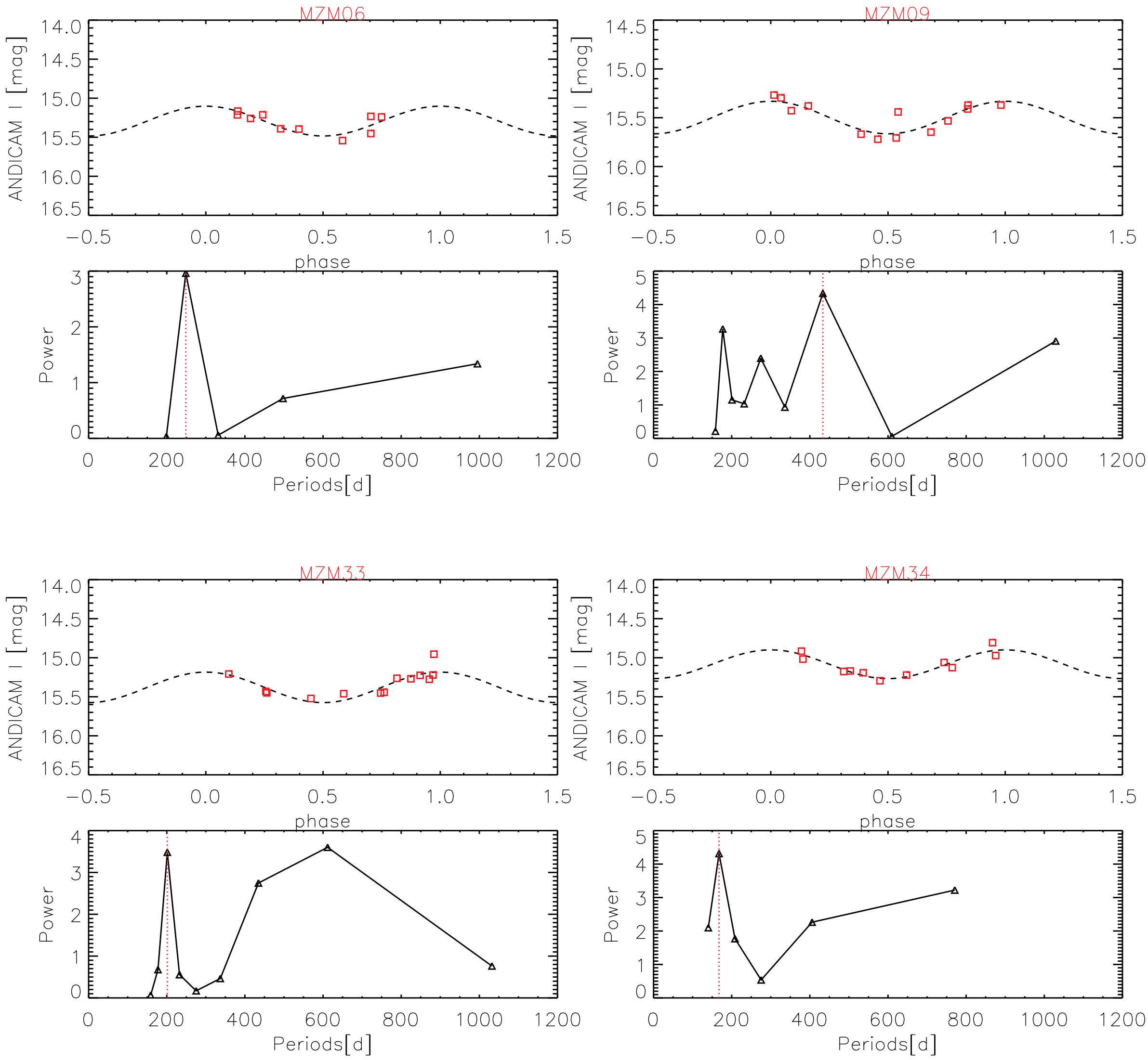

Fig. 9. For variables with an identified periodicity, *in the top panel* the sinusoidal curve vs. the phase is shown, and *in the bottom panel* the Lomb-Scargle periodogram. The red vertical dotted line marks the position of the adopted period.

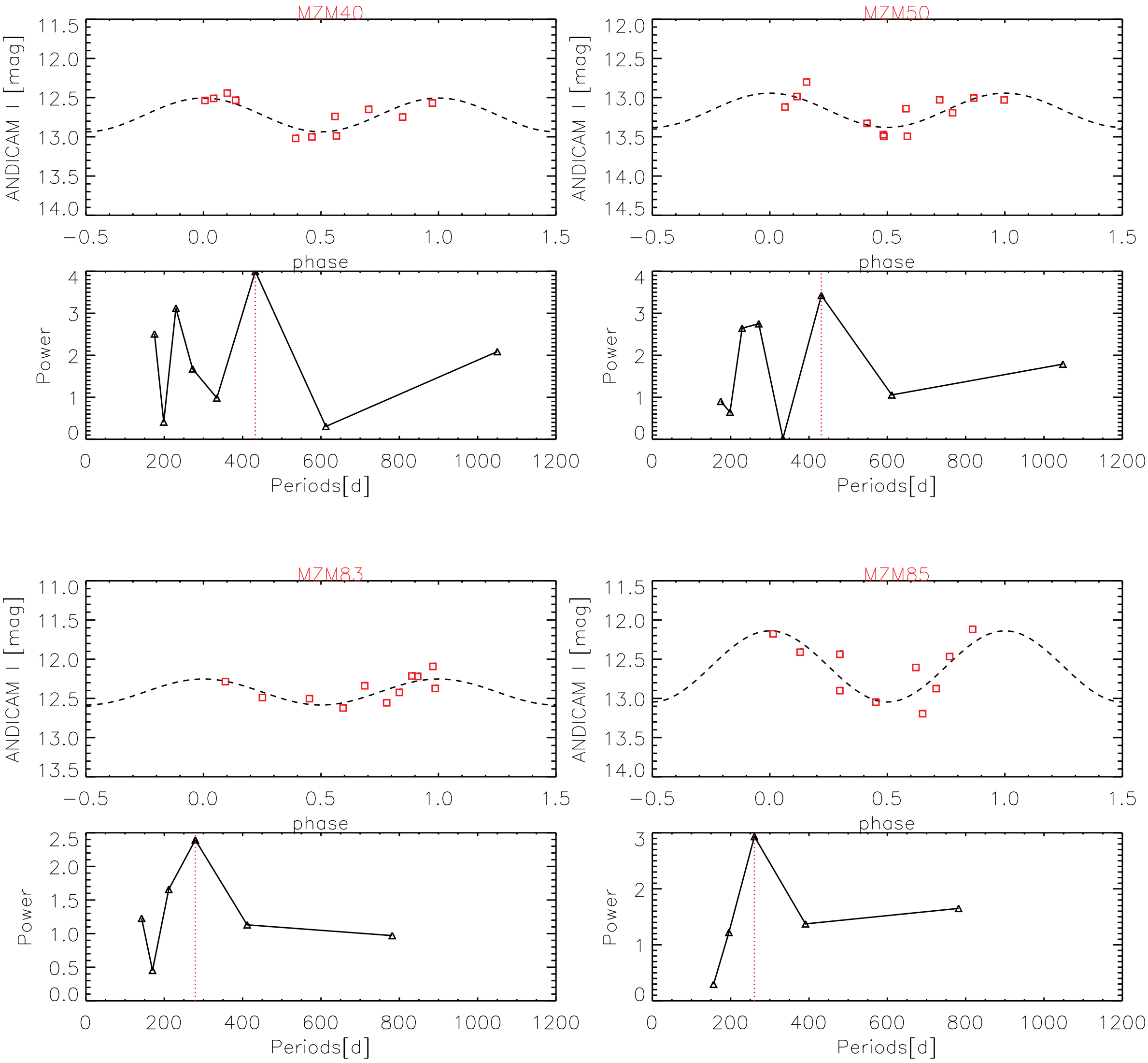

Fig. 9. Continuation of Fig. 9.

Dorda, R., Negueruela, I., & González-Fernández, C. 2018, MNRAS, 475, 2003
Drew, J. E., Gonzalez-Solares, E., Greimel, R., et al. 2014, MNRAS, 440, 2036
Epchtein, N., de Batz, B., Copet, E., et al. 1994, Ap&SS, 217, 3
Feast, M. W., Catchpole, R. M., Carter, B. S., & Roberts, G. 1980, MNRAS, 193, 377
Gaia Collaboration, Brown, A. G. A., Vallenari, A., et al. 2021, A&A, 649, A1
Glass, I. S. 1979, MNRAS, 186, 317
Horne, J. H. & Baliunas, S. L. 1986, ApJ, 302, 757
Ita, Y., Tanabé, T., Matsunaga, N., et al. 2004, MNRAS, 353, 705
Ivezić, Ž., Kahn, S. M., Tyson, J. A., et al. 2019, ApJ, 873, 111
Johnson, H. L. 1966, ARA&A, 4, 193
Kiss, L. L., Szabó, G. M., & Bedding, T. R. 2006, MNRAS, 372, 1721
Koornneef, J. 1983, A&A, 128, 84
Landolt, A. U. 2009, AJ, 137, 4186
Landsman, W. B. 1993, ASPCS, ADASS II edit. by Hanisch, R. J. and Brissenden, R. J. V. and Barnes, J., Vol. 52, The IDL Astronomy User's Library, 246
Messineo, M. & Brown, A. G. A. 2019, AJ, 158, 20
Messineo, M. & Brown, A. G. A. 2020, in Stars and their Variability Observed from Space, ed. C. Neiner, W. W. Weiss, D. Baade, R. E. Griffin, C. C. Lovekin, & A. F. J. Moffat, 111–112
Messineo, M. & Brown, A. G. A. 2021, Zenodo technical note,10.5281/zenodo.4964818
Messineo, M., Figer, D. F., Kudritzki, R.-P., et al. 2021, AJ, 162, 187
Messineo, M., Habing, H. J., Menten, K. M., Omont, A., & Sjouwerman, L. O. 2004, A&A, 418, 103
Messineo, M., Habing, H. J., Menten, K. M., et al. 2005, A&A, 435, 575
Messineo, M., Menten, K. M., Churchwell, E., & Habing, H. 2012, A&A, 537, A10
Messineo, M., Zhu, Q., Menten, K. M., et al. 2016, ApJL, 822, L5
Messineo, M., Zhu, Q., Menten, K. M., et al. 2017, ApJ, 836, 65
Mowlavi, N., Rimoldini, L., Evans, D. W., et al. 2021, A&A, 648, A44
O'Grady, A. J. G., Drout, M. R., Shappee, B. J., et al. 2021, in American Astronomical Society Meeting Abstracts, Vol. 53, American Astronomical Society Meeting Abstracts, 121.03
Pierce, M. J., Jurcevic, J. S., & Crabtree, D. 2000, MNRAS, 313, 271
Reid, M. J. & Goldston, J. E. 2002, ApJ, 568, 931
Scargle, J. D. 1982, ApJ, 263, 835
Sharma, S., Hayden, M. R., Bland-Hawthorn, J., et al. 2022, MNRAS, 510, 734
Soraisam, M. D., Bildsten, L., Drout, M. R., et al. 2018, ApJ, 859, 73
Soszyński, I. & Wood, P. R. 2013, ApJ, 763, 103

Stetson, P. B. 1987, PASP, 99, 191

Taniguchi, D., Matsunaga, N., Jian, M., et al. 2021, MNRAS, 502, 4210

VanderPlas, J. T. 2018, ApJS, 236, 16

Watson, C. L., Henden, A. A., & Price, A. 2006a, Society for Astronomical Sciences Annual Symposium, 25, 47

Watson, C. L., Henden, A. A., & Price, A. 2006b, Society for Astronomical Sciences Annual Symposium, 25, 47

Wood, P. R., Bessell, M. S., & Fox, M. W. 1983, ApJ, 272, 99

Wu, C.-J., Wu, H., Zhang, W., et al. 2021, Research in Astronomy and Astrophysics, 21, 096

Acknowledgments

An incredible amount of work was done by the CTIO/SMARTS team. This work is dedicated to a peaceful world. This work has made use of data from the European Space Agency (ESA) mission *Gaia* (*http://www.cosmos.esa.int/gaia*), processed by the *Gaia* Data Processing and Analysis Consortium (DPAC, *http://www.cosmos.esa.int/web/gaia/dpac/consortium*). Funding for the DPAC has been provided by national institutions, in particular those institutions participating in the *Gaia* Multilateral Agreement. This publication makes use of data products from the Two Micron All Sky Survey, which is a joint project of the University of Massachusetts and the Infrared Processing and Analysis Center/California Institute of Technology, funded by the National Aeronautics and Space Administration and the National Science Foundation. DENIS is a joint effort of several institutes predominantly located in Europe. It has been supported mainly by the French Institut National des Sciences de l'Univers, CNRS, and French Education Ministry, the European Southern Observatory, the State of Baden-Wuerttemberg, and the European Commission under networks of the SCIENCE and Human Capital and Mobility programs, the Landessternwarte, Heidelberg and Institut d'Astrophysique de Paris. The Pan-STARRS1 Surveys (PS1) and the PS1 public science archive have been made possible through contributions by the Institute for Astronomy, the University of Hawaii, the Pan-STARRS Project Office, the Max-Planck Society and its participating institutes, the Max Planck Institute for Astronomy, Heidelberg and the Max Planck Institute for Extraterrestrial Physics, Garching, The Johns Hopkins University, Durham University, the University of Edinburgh, the Queen's University Belfast, the Harvard-Smithsonian Center for Astrophysics, the Las Cumbres Observatory Global Telescope Network Incorporated, the National Central University of Taiwan, the Space Telescope Science Institute, the National Aeronautics and Space Administration under Grant No. NNX08AR22G issued through the Planetary Science Division of the NASA Science Mission Directorate, the National Science Foundation Grant No. AST-1238877, the University of Maryland, Eotvos Lorand University (ELTE), the Los Alamos National Laboratory, and the Gordon and Betty Moore Foundation. VPHAS+ is based on observations made with ESO Telescopes at the La Silla or Paranal Observatories under programme ID(s) 177.D-3023(B), 177.D-3023(C), 177.D-3023(D), 177.D-3023(E). This research has made use of the VizieR catalog access tool, CDS, Strasbourg, France, and SIMBAD database. This research has made use of NASAs Astrophysics Data System Bibliographic Services (ADS). This work was partially supported by the National Natural Science Foundation of China (NSFC-11773025), and USTC start-up grant KY2030000054.